

Article

A Comprehensive Study of LFP-Based Positive Electrodes: Process Parameters' Influence on the Electrochemical Properties

Beatriz Arouca Maia ^{1,2,3,4} , Natália Magalhães ¹ , Eunice Cunha ¹ , Nuno Correia ^{1,4}, Maria Helena Braga ^{2,3,4,*}  and Raquel M. Santos ^{1,4,*} 

¹ Materials and Composite Structures Unit (UMEC), Institute of Science and Innovation in Mechanical and Industrial Engineering (INEGI), 4200-465 Porto, Portugal; bmaia@inegi.up.pt (B.A.M.); natalia.5393@gmail.com (N.M.); ecunha@inegi.up.pt (E.C.); ncorreia@inegi.up.pt (N.C.)

² Faculty of Engineering, University of Porto, 4200-465 Porto, Portugal

³ Materials for Energy Research Laboratory (MatER), University of Porto, 4200-465 Porto, Portugal

⁴ Associated Laboratory of Energy, Transports and Aerospace (LAETA), 4200-265 Porto, Portugal

* Correspondence: mbraga@fe.up.pt (M.H.B.); rmsantos@inegi.up.pt (R.M.S.)

Abstract: This study explores the preparation of lithium iron phosphate (LFP) electrodes for lithium-ion batteries (LIBs), focusing on electrode loadings, dispersion techniques, and drying methods. Using a three-roll mill for LFP slurry dispersion, good electrochemical properties were achieved with loadings of $5\text{--}8 \text{ mg}\cdot\text{cm}^{-2}$ ($0.8\text{--}1.2 \text{ mAh}\cdot\text{cm}^{-2}$ areal capacity). Adding polyvinylidene fluoride (PVDF) during the final milling stage reduced performance due to premature solidification in-between rolls. Vacuum-free drying improved ionic conductivity, stability against lithium metal, and discharge capacity, whereas vacuum-dried samples exhibited higher initial resistance and lower capacity retention. These findings highlight critical parameters for enhancing LFP electrode performance, paving the way for high-performance, and sustainable energy-storage solutions.

Keywords: LFP-based positive electrodes; energy-storage systems; process parameters; dispersion techniques; electrochemical performance



Academic Editor: George Zheng Chen

Received: 15 January 2025

Revised: 22 February 2025

Accepted: 24 February 2025

Published: 27 February 2025

Citation: Arouca Maia, B.; Magalhães, N.; Cunha, E.; Correia, N.; Braga, M.H.; Santos, R.M. A Comprehensive Study of LFP-Based Positive Electrodes: Process Parameters' Influence on the Electrochemical Properties. *Batteries* **2025**, *11*, 93. <https://doi.org/10.3390/batteries11030093>

Copyright: © 2025 by the authors. Licensee MDPI, Basel, Switzerland. This article is an open access article distributed under the terms and conditions of the Creative Commons Attribution (CC BY) license (<https://creativecommons.org/licenses/by/4.0/>).

1. Introduction

The advent of wireless devices has promoted the study of novel energy-storage systems (ESS). The intense competition for obtaining efficient ESS that fulfill the growing requirements of ever more demanding applications has catalyzed remarkable scientific advancements in a short timeframe [1]. The echoes of the overexploitation of natural resources and the fossil fuel crisis are driving forces toward the decarbonization of energy production and storage. Replacing fossil fuels with renewable sources is the first step for achieving carbon neutrality in 2050, in accordance with the European Commission. The application of ESS, namely with battery systems, became the go-to solution [2,3].

Lithium-ion batteries (LIBs) have played a vital role in the energy sector, especially when electric mobility is no longer a chimera [4]. LIBs have been employed in small and portable electronics, such as laptops and smartphones, hybrid and electric vehicles, and even grid-connected ESS [5,6]. LIBs can reach a specific energy of approximately $250 \text{ Wh}\cdot\text{kg}^{-1}$ at the cell level and allow for a driving range of 300–600 km [7]. Therefore, according to the global vehicle market expectations, the sale of LIBs for electric vehicles will increase from 70 million in 2020 to 180 million by 2045 [8].

In addition, LIBs offer good energy allied to high power densities, low maintenance, safety, long service life, and reasonable operating voltage, providing excellent properties

for several applications [9,10]. Although there was a steady rise in the global production of LIBs in the past decade, especially in non-western countries, their energy density has shown slow progress [11]. It is broadly accepted that employing a high-voltage positive electrode is a simple and powerful approach for improving the energy density of LIBs, since positive electrodes usually limit both the operating voltage and capacity [12–14]. Four main categories encompass suitable candidates for positive-electrode materials, including the Li transition metal oxides family LiMO_2 ($M = \text{Co}, \text{Ni}, \text{Mn}$ among others), Li manganese spinel LiMn_2O_4 , the nickel-rich layered oxides ($\text{LiNi}_x\text{Co}_y\text{Mn}_z\text{O}_2$ with $x + y + z = 1$), and Li polyanion compound family $(\text{Li}_x\text{M}_y)(\text{AO}_4)_z$ (where $M = \text{Co}, \text{Mn}, \text{Fe}, \text{V}, \dots, A = \text{S}, \text{Si}, \text{P}, \dots$, with $x + y + z = 1$) [15–17]. Lithium iron phosphate (LiFePO_4), generally referred to as LFP, was first discovered by Padhi et al. [18] after recognizing the polyanion classification by Professor John Goodenough [19,20].

LFP-based electrode slurries are usually produced by using three main components: (i) active material, (ii) polymer binder, and (iii) carbon material to provide electron conductivity. The most-used polymer is polyvinylidene fluoride (PVDF), a material with good mechanical and (electro)chemical properties, along with carbon black (CB), acting as the carbon source [21].

LFP has prompted significant interest owing to its availability, stable cyclability, and environmentally friendly composition, compared to the nickel-rich layered oxides (NMC) [22–24]. Furthermore, the material shows considerable cycle stability, robust safety features, and a competitive theoretical discharge capacity of $\approx 170 \text{ mAh}\cdot\text{g}^{-1}$. As a mature, cost-effective technology with scalable production, LFP is also suitable for applications where solid-state electrolytes are still in development [25]. Nevertheless, LFP also exhibit low electrical and ionic conductivities and, therefore, a low ionic diffusion coefficient ($10^{-11} \text{ S}\cdot\text{cm}^{-1}$ and $10^{-14} \text{ cm}^2\cdot\text{s}^{-1}$, respectively) [14,26].

In this context, several attempts have already been made to surpass these challenges by: (i) using different production processes [27–29], (ii) optimizing process parameters [30,31], (iii) employing carbon allotropes to increase the positive electrode's electrical conductivity [32], or (iv) adding heterostructures to increase ionic conductivity [33]. Numerous studies have focused on the state, kinetics, and dispersion mechanisms of carbon-based nanomaterials added to the active materials' slurries instead of conventional carbon black [34–38].

This study aimed to understand the impact of electrode-processing parameters by analyzing the electrochemical performance of LFP-based positive electrodes at room temperature (RT). The primary goal is not to demonstrate stable performance over extended cycles but rather to explore and understand how different factors—including dispersion techniques, and drying methods—affect the performance of LFP-based cells. In this context, preliminary studies were conducted to explore the influence of an intensive mixer (three-roll milling), which can generate high hydrodynamic shear stresses, on particle dispersion and stability and, subsequently, on the electrochemical performance of the electrode. According to the literature, this approach was only tested with different types of positive electrodes, which included carbon nanotubes [39]. In addition, a comprehensive examination encompassed an evaluation of different electrode loadings (low, medium, and high loadings), and drying methods to determine their impact on cyclability and discharge capacity. Moreover, a systematic approach was employed to confirm if further enhancements were possible by optimizing steps during the dispersion stage. To the best of our knowledge, we show an innovative approach to the study of LFP-based positive electrodes where the work is focused on the extensive use of a three-roll mill for dispersion while testing different process parameters. This study revealed that dispersion was pivotal in determining the ultimate electrochemical performance. It was found that loadings between 5 and $8 \text{ mg}\cdot\text{cm}^{-2}$ (0.8 to $1.2 \text{ mAh}\cdot\text{cm}^{-2}$ areal capacity) and dried without vacuum exhibited good behavior across

a spectrum of methods and current rates. These positive electrodes demonstrated robust stability and delivered high discharge capacities, confirming enhanced performance.

2. Materials and Methods

2.1. Materials

Lithium iron phosphate LiFePO₄, with a particle size between 0.5 and 1.5 μm , 1.132 g·cm⁻³ tap density and practical (in the technical datasheet) discharge capacity of 155.5 mAh·g⁻¹; carbon black CB, 35–50 nm particle size; and polyvinylidene fluoride PVDF, molecular weight distribution of 600,000 were purchased from Nanografi® (Ankara, Turkey). The solvent used for the positive electrode slurries was N-methylprolidone (NMP), obtained from Merck® (Darmstadt, Germany). To cast the resulting slurries, a carbon-coated aluminum foil with a total thickness of 20 μm was used, also from Nanografi®.

CR2032 coin-cell constituents, including aluminum and copper foils, as well as the stainless-steel positive and negative caps, springs, and spacers, were all purchased from Nanografi®. The liquid electrolyte in this study was a 1.0 M solution of lithium hexafluorophosphate LiPF₆ in a 50:50 (*v/v*) mixture of ethylene carbonate and dimethyl carbonate (EC:DMC), purchased from Merck®. The glass-fiber (GF) separator with 0.67 mm of thickness was obtained from Whatman®, Merck®.

2.2. Preparation and Optimization of LiFePO₄ Conventional Positive Electrode Slurry

In pursuit of understanding the process parameters' effect on the electrochemical properties, a comprehensive analysis of the various factors influencing LFP positive electrode fabrication was assessed, where the formulation of the prepared cathodes was kept at 80 wt.% LFP, 10 wt.% CB, and 10 wt.% PVDF. The employed methods explored three different electrode loadings—ranging from <5 to >8 mg·cm⁻² (<0.78 to >1.24 mAh·g⁻¹ areal capacity). The impact of the drying method was additionally evaluated. These loadings were achieved by using a doctor blade with a 100 μm gap. To adjust the electrode loading, the amount of NMP solvent was varied accordingly—using less solvent for higher loadings and more solvent for lower loadings. All electrode loadings were prepared by mixing 8 g of LFP, 1 g of PVDF, and 1 g of CB in NMP solvent. Specifically, to achieve a low electrode loading 25 mL of NMP solvent was used, and for medium and high loadings such as 7 and 9 mg·cm⁻², the employed NMP solvent was 20 mL and 15 mL, respectively (please see Table S1 in the Supplementary Materials). The thicknesses of the positive electrodes' final sheets, after drying, were confirmed with a micrometer (please see Figure S1 in the Supplementary Materials).

A series of experiments were conducted to explore how the dispersion process influenced the discharge capacity. A three-roll mill EXAKT 80 from EXAKT Technologies, Inc.® (Oklahoma City, OK, USA) was used to ensure an effective particle dispersion, and three different methods, A, B, and C, were tested. The difference between approaches is represented in Figure 1 for Methods A and B, and Figure 2 for Method C.

Three different stages were applied to attain homogeneous dispersions which had different feed-to-central (δ_1) and central-to-apron (δ_2) roll gaps, and the material was forced to pass through the feed roll three times [40]. The gaps between each roll and the rolls' velocities were detailed elsewhere [40].

In Method A (Figure 1a), PVDF was first dissolved in NMP. Separately, CB and LFP were dispersed in NMP, and processed using three-roll mill equipment. Once this dispersion was complete, it was added to the PVDF + NMP mixture. That is, after the initial dispersion of CB, LFP, and NMP, the resulting slurry was combined with the PVDF+NMP solution and then reintroduced into the milling rolls for further processing.

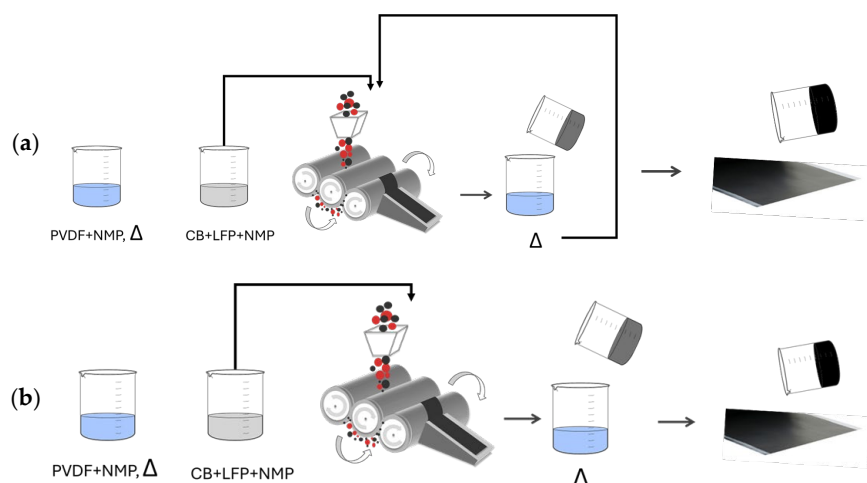


Figure 1. Investigated routines for three-mill dispersion. (a) the polymer was prepared separately and only CB, LFP, and NMP were introduced in the three-roll mill (Method A); after mixing the dispersion and mixture, the resulting slurry was reintroduced in the three-roll mill. (b) The resulting slurry was not reintroduced in the three-roll mill (Method B).

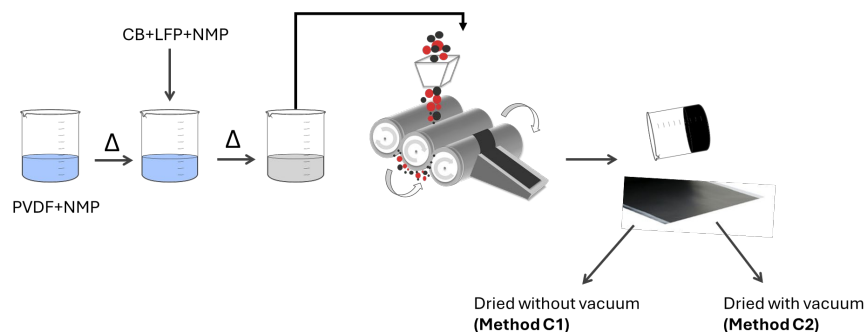


Figure 2. Investigated routine to optimize three-mill dispersion by adding the slurry into the milling-machine and a further evaluation of the drying process. In Method C1 (=C), the positive electrode dried as in Methods A and B, and in Method C2, the positive electrode dried in vacuum.

The final slurry (LFP + CB + PVDF + NMP) was cast onto the carbon-coated aluminum (Al) foil using a high-precision doctor blade micrometer, to ensure a 100 μm uniform thickness in all the positive electrodes. The samples were then dried in a furnace at 70 $^{\circ}\text{C}$. Before coin-cell assembly, the samples were placed into the antechamber of the glovebox, where the temperature was set to 40 $^{\circ}\text{C}$ under an argon atmosphere for one hour, and subsequently stored inside the glovebox. The thickness was re-confirmed using a micrometer. In Method B (Figure 1b), the first and last steps were equivalent to Method A, but the final mixture was not added again to the milling equipment.

To further evaluate if the three-roll mill process was being carried out effectively, a new approach was tested (Method C), represented in Figure 2, where the slurry with all the components prepared in sequence, PVDF + NMP then CB + LFP + NMP, was added into the milling machine. Further evaluation aiming at studying the influence of the drying process on the electrochemical properties of LFP-based positive electrodes was attained with Methods C1 (control of Method C) and C2, shown in Figure 2.

The LFP-based electrodes were prepared and studied using a coin-cell configuration, as shown in Figure 3.

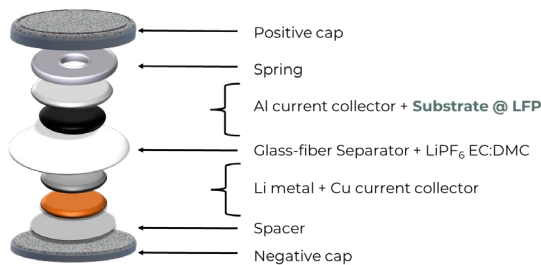


Figure 3. Coin-cell configuration used to study the behavior of LFP-based electrodes. The substrate is carbon-coated aluminum foil.

CR2032 coin-cells were assembled in an argon-filled glovebox ($O_2 < 2$ ppm, $H_2O < 0.8$ ppm). Aluminum and copper (Cu) foils were used as the positive and negative current collectors, respectively. The LFP-based electrode was used as the positive electrode and Li-metal as the counter-electrode. A volume of $70\ \mu L$ of $LiPF_6$ EC:DMC electrolyte solution was dropped onto the positive electrode side. The diameters of each coin-cell component are specified in Table 1.

Table 1. Diameters for each coin-cell component.

Stainless Steel Spring	Al Current Collector	LFP Positive Electrode	GF Separator	Li Negative Electrode	Cu Current Collector	SS Spacer
15.4 mm	15 mm	15 mm	18 mm	16 mm	10 mm	15.8 mm

2.3. Characterization

Aiming to investigate the electrochemical performance of the LFP positive electrodes, electrochemical impedance spectroscopy (EIS), cyclic voltammetry (CV), and galvanostatic charge and discharge cycles were conducted. To ensure the reliability of the results, all cells produced were stabilized at RT (≈ 23 °C) for 24 h before undergoing testing with the LFP//Li-metal configuration. EIS tests were performed at RT in a BioLogic VMP-300 potentiostat (Bio-Logic Science Instruments, Seyssinet-Pariset, France), from 1.0×10^6 to 1.0×10^{-1} Hz, with an alternating current (AC) potential amplitude of ± 100 mV, and all the experiments and the corresponding parameters obtained from the equivalent circuit are listed in Table S2 in Supplementary Materials. The EIS experiments were performed before charging the cells for the first time. Since the applied AC amplitude is small (± 100 mV), it is expected that most activity will be at the positive electrode side, as shown before in [1]. The data were analyzed, calculating the capacitances and resistances of the equivalent circuit composed by an inductor L_1 in series with a resistor R_1 with a parallel of a non-ideal capacitor and a resistor R_2 [41]. The resistor R_1 corresponds to the ohmic resistance with no direct correspondence in both electrodes and sums up both cationic and anionic contributions with the liquid electrolyte. The resistor R_2 corresponds to the ionic transport resistance of the double-layer capacitor (EDLC) formed at the interface electrode/electrolyte to equalize, dynamically, the electrochemical potentials of species in contact. Z_M is the anomalous diffusion impedance associated in series to the previous elements, corresponding to the “tail” of the semicircle at the lowest frequencies [42–44], according to:

$$Z_M = R_3 \frac{\coth(\tau_3 \omega j)^{\frac{\gamma_3}{2}}}{(\tau_3 \omega j)^{\frac{1-\gamma_3}{2}}} \quad (1)$$

where R_3 is the corresponding resistance, τ_3 is the time constant, $\omega = 2\pi f$, f the frequency of the AC signal, and γ_3 a dimensionless optimizable parameter that measures the deviation from the ideality (corresponding to a 45° phase). A phase angle of 45° in the Nyquist plot is

characteristic of ideal semi-infinite diffusion, where the Warburg impedance is dominant. If the phase is not 45° , it may indicate deviations from ideal diffusion, such as: (a) finite-length diffusion, (b) interfacial effects that modify the diffusion process, and (c) non-uniform or constrained diffusion pathways.

If the diffusion process is restricted, such as in thin films, porous electrodes, or limited geometries, the phase angle may deviate from 45° . This behavior is described by a finite-length Warburg impedance, where the transition from diffusion-limited behavior occurs earlier. A phase angle different from 45° could also result from additional processes occurring in parallel with diffusion, including: (a) charge transfer resistance, (b) adsorption/desorption phenomena, and (c) double-layer capacitance effects. Factors like rough electrode surfaces, heterogeneous reaction sites, or varying electrolyte conductivity can distort the expected impedance response, leading to a non- 45° phase angle.

In some systems, the impedance at low frequencies may represent a mix of diffusion and reaction kinetics, leading to a phase angle that lies between those characteristics of purely diffusion-controlled (45°), and reaction-controlled (0° or 90°) processes.

Therefore, the ionic conductivity at the positive electrode can be calculated from:

$$R_3 = \frac{1}{\sigma} \frac{l}{A} \quad (2)$$

where R_3 is the resistance of the positive electrode in Ω , σ is the ionic conductivity in $S \cdot cm^{-1}$, l is the diffusion pathway of the positive electrode in cm which, herein, is considered the thickness of the positive electrode $100 \pm 1 \mu m$, and A is the surface area of the electrode in cm^2 [6,45]. The theoretical fit parameters are represented in Supplementary Materials, Table S2.

Cyclic voltammetry (CV) was also performed in a BioLogic VMP-300 at a scan rate of $5 \text{ mV} \cdot \text{s}^{-1}$ and RT, aiming to understand the electrochemical stability in a pre-determined voltage range.

Galvanostatic cycles were conducted on a Neware battery tester (Shenzhen, China) at RT, between 2.8 and 3.8 V, suitable for LFP electrodes. Different C-rates were employed, from $C/20$ to C . The C-rates were calculated in accordance with the reversible capacity given on the technical datasheet ($155.5 \text{ mA} \cdot \text{h} \cdot \text{g}^{-1}$) [39]. The areal capacities were calculated using this capacity value. During the charge step, a constant-current constant-voltage mode for a cut-off of 3.8 V was used. During the discharge, the constant-current mode was employed with a voltage limit of 2.8 V and a capacity limit of $170 \text{ mA} \cdot \text{h} \cdot \text{g}^{-1}$ (corresponding to the theoretical capacity of LFP-based electrodes).

Scanning electron microscopy (SEM) was used to analyze the morphology of the developed positive electrodes at different magnifications. Samples were sputter-coated with a mixture of gold/palladium (Au/Pd) for 100 s.

3. Results

3.1. Effect of the Dispersion Routine (Method A and B)

An overview of the literature shows that traditional positive-electrode slurries are mainly obtained by physical mixture either magnetic or mechanical agitation of their components [28–30]. In this work, the positive-electrode samples were prepared under higher hydrodynamic shear stresses (three-roll mill) to observe differences in dispersion and morphology.

The electrode loadings and corresponding areal capacities are depicted in Table 2.

Table 2. Evaluation of the dispersion protocols. Methods A vs. B at different electrode loadings/areal capacities.

Method	Low Loading (<5 mg·cm ⁻²)			Medium Loading (6–8 mg·cm ⁻²)			High Loading (>8 mg·cm ⁻²)		
	Sample #	Loading (mg·cm ⁻²)	Estimated Areal Capacity (mA·h·cm ⁻²)	Sample #	Loading (mg·cm ⁻²)	Estimated Areal Capacity (mA·h·cm ⁻²)	Sample #	Loading (mg·cm ⁻²)	Estimated Areal Capacity (mA·h·cm ⁻²)
A	A1	5.53	0.86	A3	7.47	1.16	A5	9.78	1.52
	A2	6.21	0.96	A4	7.56	1.18	A6	13.04	2.03
B	B1	5.34	0.83	B3	6.39	0.99	B5	8.06	1.25
	B2	5.34	0.83	B4	6.88	1.07	B6	8.42	1.31

The main purpose of this study was to evaluate the effectiveness of the dispersion protocol, and determine whether modifications could enhance both the dispersion quality and the resulting electrochemical properties. It is important to note that all samples were prepared with the same coating thickness of $100 \pm 1 \mu\text{m}$, ensuring that the electrode loading and preparation method are the key distinguishing factors in analysis. Increasing LFP loading also increases the electrode density for electrodes with the same thickness.

In Method A, the samples were prepared by dissolving PVDF in NMP (at 60 °C), and, in a separate container CB and LFP in NMP, at RT. Once the PVDF was completely dissolved, the suspension containing CB and LFP was introduced into a three-roll mill. The dispersion was then placed into the PVDF beaker under agitation, which fed the milling equipment for another passage.

The first point to highlight is that when the final slurry (CB + LFP + PVDF) was introduced into the milling rolls, the PVDF began to precipitate onto the rolls, as shown in Figure 4. This finding was a concern, since it indicates inadequate dispersion methodology, which could negatively impact the electrochemical outcomes, giving rise to heterogeneous performances. This effect occurred due to the evaporation of NMP, promoting PVDF precipitation due to the friction from the milling rolls. Furthermore, and because of the uneven dispersion, it was challenging to achieve consistent electrode loading. Therefore, sample A2 with a loading of $6.21 \text{ mg}\cdot\text{cm}^{-2}$ ($0.96 \text{ mA}\cdot\text{h}\cdot\text{cm}^{-2}$), was still classified as a low-loading sample.



Figure 4. Evidence of PVDF precipitation on the milling roll equipment.

Since the dispersion of materials was inadequate, the obtained results are not coherent. Therefore, the influence of the dispersion routine in Method A on the EIS, CV and cycling profiles are presented in Figure S3, in the Supplementary Materials. In a tentative bid to optimize the dispersion method, a new dispersion routine was tested in Method B.

In this case, the samples were prepared by dissolving PVDF in NMP (at 60 °C), and, in a separate container, CB and LFP in NMP at RT. Once the PVDF was completely dissolved, the suspension containing CB and LFP was introduced into the three-roll mill. The dispersion was then placed into the PVDF beaker under agitation, and the final slurry was used to cast carbon-coated aluminum foils to produce LFP-based positive electrodes. An enhanced dispersion was obtained within this method, as shown in Figure 5.

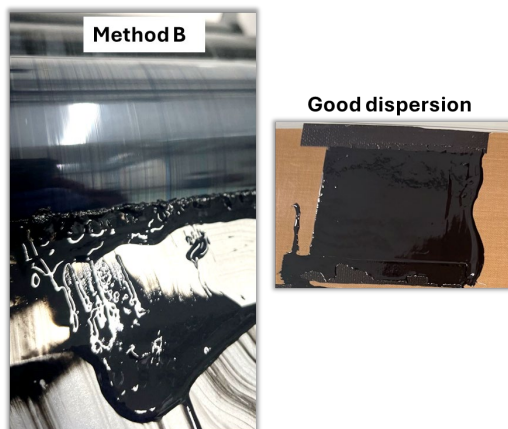


Figure 5. Practical evidence of enhanced dispersion within Method B.

The process for assembling coin cells is similar to the one previously described for Method A, and the EIS and CV profiles are shown in Figure 6.

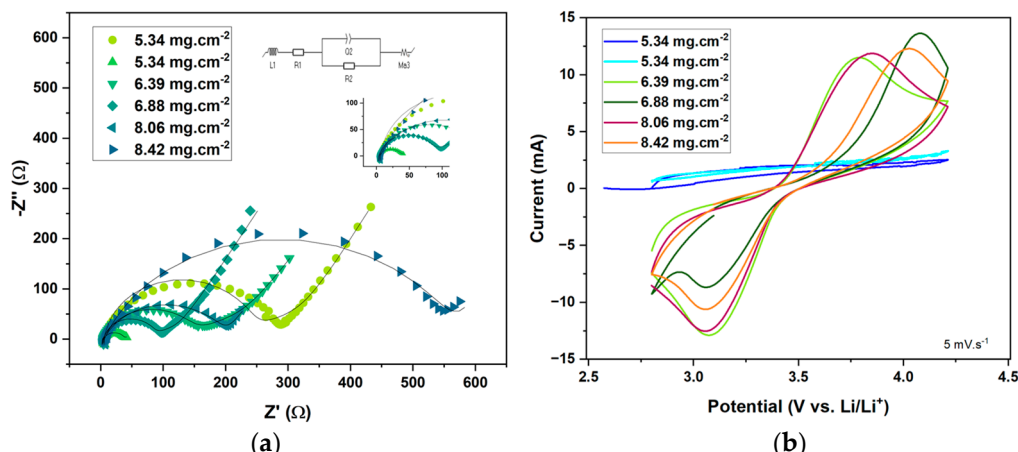


Figure 6. Electrochemical performance for the Method B B1–6 samples with positive-electrode loads varying from 5.34 mg.cm^{-2} to 8.42 mg.cm^{-2} (0.83 to $1.31 \text{ mA}\cdot\text{h}\cdot\text{cm}^{-2}$). (a) EIS and (b) CV.

The EIS and CV experiments were conducted prior to the first charge. In Figure 6a, a depressed semicircle in the high-frequency region and a sloping line in the low-frequency region domain constitute the Nyquist plot. The positive electrodes' resistances obtained from R_3 in Equation (1) were 270, 1148, 267, 133, 59, and 87Ω , for B1–6, resulting in ionic conductivities of 0.07, 0.02, 0.07, 0.1, 0.3, and $0.2 \text{ mS}\cdot\text{cm}^{-1}$. It is highlighted that a lower overall impedance does not necessarily mean a higher positive-electrode ionic conductivity. The increased electrode loading/areal capacity led, overall, to higher ionic conductivities. The grayish lines represent the theoretical fit of each curve, and the details can be consulted in Table S2 (see Supplementary Materials). The voltammograms in Figure 6b were performed at $5 \text{ mV}\cdot\text{s}^{-1}$ and RT. Lower electrode loadings could not handle higher currents and the best compromise was obtained for the samples with medium and high loadings, showcasing the profile for an LFP type of cell, with the peaks well pronounced at

the characteristic intercalation and deintercalation reaction potentials. After CV analysis, the cells were subjected to galvanostatic cycling, shown in Figure 7.

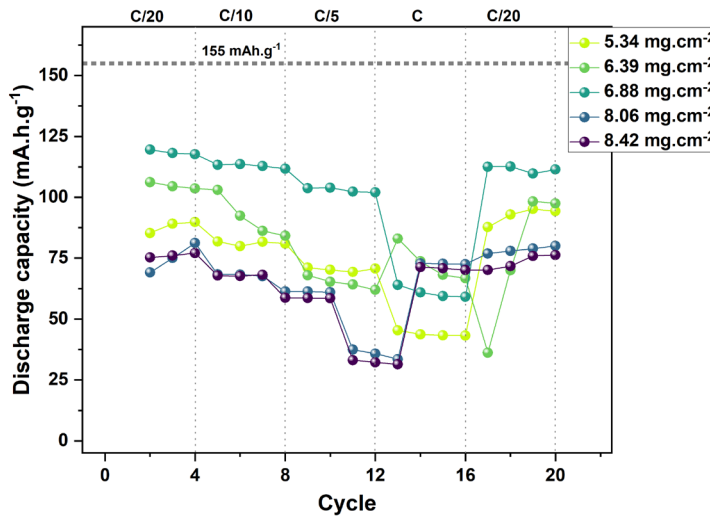


Figure 7. Comparative C-rate capabilities for the samples prepared by Method B. The positive electrode with $5.34 \text{ mg}\cdot\text{cm}^{-2}$ corresponds to B1.

Electrochemical cycling at different C-rates demonstrated greater stability with medium loadings, though the theoretical capacities were not reached (Figure 7).

The B2 sample demonstrated poor electrochemical performance, particularly in electrochemical capacities. Its discharge capacity did not exceed $8 \text{ mA}\cdot\text{h}\cdot\text{g}^{-1}$, indicating high internal resistance and poor dispersion of the positive-electrode material, explaining its removal from further characterization. The latter reinforces that lower overall impedance does not necessarily mean higher positive-electrode conductivity (it is the lowest in this case, $\sigma_{B2} = 0.02 \text{ mS}\cdot\text{cm}^{-1}$), and better electrochemical performance (it was the worst, not exceeding $8 \text{ mA}\cdot\text{h}\cdot\text{g}^{-1}$).

On the other hand, and even though B4 sample ($6.88 \text{ mg}\cdot\text{cm}^{-2}$) did not reach the theoretical capacity, it outperformed the other samples at almost all the C-rates, except for 1C step, and it reached $111.4 \text{ mA}\cdot\text{h}\cdot\text{g}^{-1}$ by the end of the final C/20 scan, retaining 93% of its initial capacity. The samples with higher loadings were able to stabilize at 1C, remaining at almost $90 \text{ mA}\cdot\text{h}\cdot\text{g}^{-1}$ until the end of the scanning.

The Coulombic efficiency can be consulted in Figure S4a (see Supplementary Materials). Compared to Method A, this routine demonstrated improved results with much improved electrochemical cycling performance, although not achieving full practical capacity. However, it remains unclear whether further optimization is possible. This highlights the importance of investigating potential enhancements through modifications to the milling roll process, ensuring clear evidence that the process is being executed accurately.

3.2. Effect of the Dispersion Routine (Method C) and Drying Method (Methods C1 and C2)

The method discussed in this section, Method C, involved the dissolution of PVDF in NMP at 60°C and 400 rpm, while CB and LFP were separately dispersed in NMP. The resultant dispersion was subsequently combined to the PVDF solution under magnetic agitation. This final mixture underwent dispersion by using the three-roll mill and the resulting slurry was then deposited onto a carbon-coated aluminum substrate (Method C). An evaluation was conducted to determine whether employing vacuum drying could yield improved results leading to the control Method C = C1 (without vacuum) and the vacuum-drying Method C2.

This process yielded twelve distinct batches, and the respective electrode loadings of each batch are detailed in Table 3.

Table 3. An assessment of the drying method and electrode loading/areal capacity influence on the electrochemical behavior of the produced positive electrodes, from Method C. In Method C = C1, it was used a conventional oven, and in Method C2, it was applied vacuum in a dedicated vacuum oven.

Method	Low Loading (<5 mg·cm ⁻²)			Medium Loading (6–8 mg·cm ⁻²)			High Loading (>8 mg·cm ⁻²)		
	Sample #	Loading (mg·cm ⁻²)	Estimated Areal Capacity (mA·h·cm ⁻²)	Sample #	Loading (mg·cm ⁻²)	Estimated Areal Capacity (mA·h·cm ⁻²)	Sample #	Loading (mg·cm ⁻²)	Estimated Areal Capacity (mA·h·cm ⁻²)
C1	C1.1	3.26	0.51	C1.3	6.30	0.98	C1.5	7.84	1.22
	C1.2	5.53	0.86	C1.4	6.34	0.99	C1.6	9.24	1.44
C2	C2.1	4.57	0.71	C2.3	6.11	0.95	C2.5	7.65	1.19
	C2.2	5.03	0.78	C2.4	6.88	1.07	C2.6	9.24	1.44

SEM was performed to analyze the samples' surface topology and assess whether different outcomes arise from the use of vacuum drying. In Figure 8, the surface morphology of two representative samples within the same loading range is shown, from Methods C1 and C2.

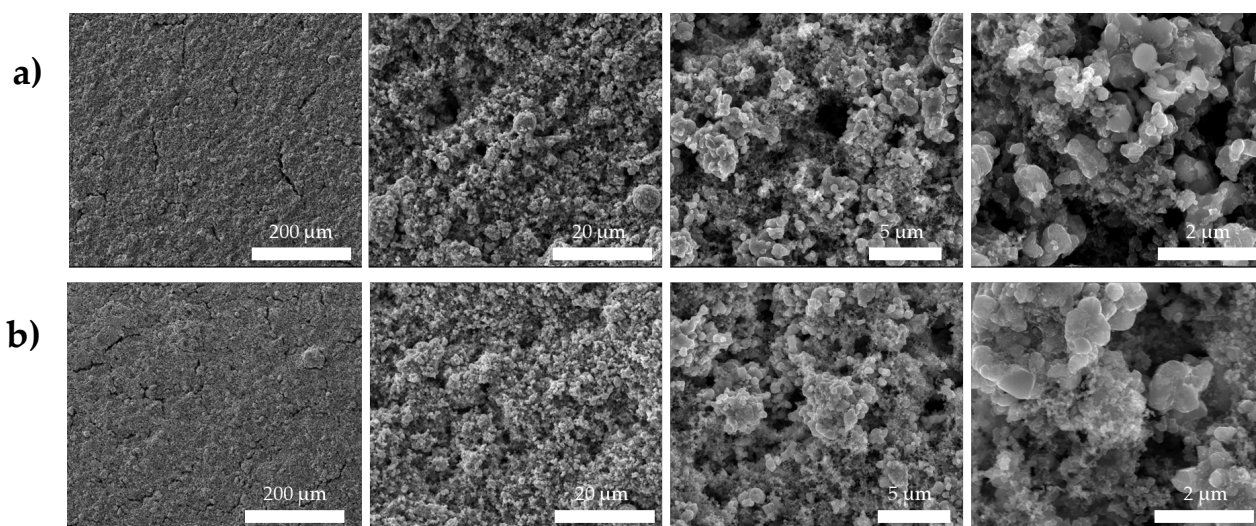


Figure 8. SEM surface images of LFP-based positive electrodes with (a) 6.30 mg·cm⁻² (Method C = C1) and (b) 6.88 mg·cm⁻² (Method C2) mass loadings, for magnifications of 500 \times , 5000 \times , 15,000 \times , and 50,000 \times .

The LFP-based positive electrodes show a similar appearance of agglomerated particles with narrow size distribution. The impact of the drying technique is not clearly observed, since both positive electrodes show the same morphology. In Figure S2, a comparison of the LFP-positive-electrode surface of samples prepared by magnetic agitation and three-roll mill is depicted, from which it is concluded that the milling roll promotes a more uniform particle size.

To understand the milling roll effect and the drying technique on the electrochemical properties in depth, a series of electrochemical characterizations was conducted. In Figure 9, the EIS and CV data for Methods C1 and C2 are represented.

All EIS and CV experiments were conducted before cycling. In Figure 9a, the Nyquist plot for the samples prepared by Method C1, as well as a zoom-in of the high-frequency region are shown. The grayish lines represent the theoretical fitting of the Nyquist curves, and the related parameters are summarized in Supplementary Materials, Table S2. The EIS

shows that the resistances of the samples C1.1 to C1.6 calculated from Equation (1) were 12, 132, 4, 7, 5, and 6 Ω , corresponding to the ionic conductivities of 1.4, 0.1, 4.4, 2.4, 1.3, and 2.8 $\text{mS}\cdot\text{cm}^{-1}$, respectively, assuming that the diffusion pathway of the positive electrode (l) in Equation (2) is its thickness of $100 \pm 1 \mu\text{m}$. The tendency of these results shows that the best ionic conductivities were obtained with positive electrodes with medium to high loadings, as predicted in the literature [46,47].

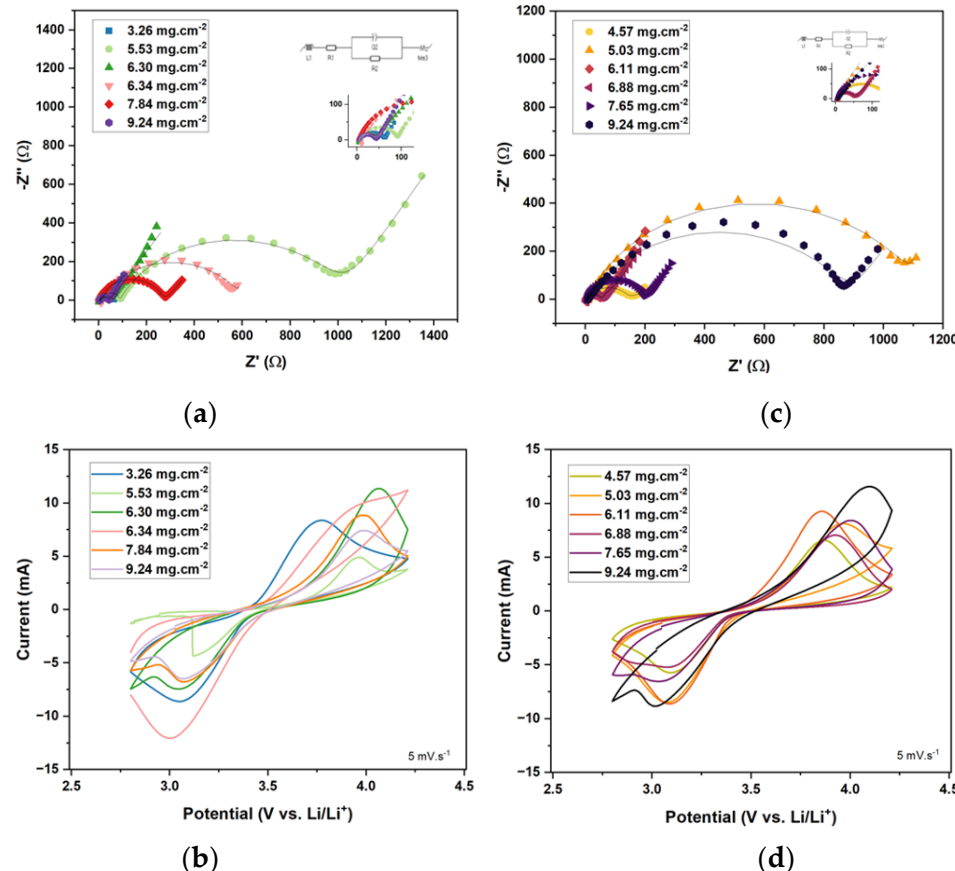


Figure 9. Electrochemical analyses: (a) EIS and (b) CV for samples prepared by Method C1 (control Method C), ranging from 3.26 to $9.24 \text{ mg}\cdot\text{cm}^{-2}$ positive-electrode loading (0.51 to $1.44 \text{ mA}\cdot\text{h}\cdot\text{cm}^{-2}$); (c) EIS and (d) CV, for samples prepared by Method C2, ranging from 4.57 to $9.24 \text{ mg}\cdot\text{cm}^{-2}$ positive-electrode loading (0.71 to $1.44 \text{ mA}\cdot\text{h}\cdot\text{cm}^{-2}$).

Considering the reversibility and stability study, the same samples were subjected to CV testing and the results are shown in Figure 9b. The CVs were conducted prior to cycling and after EIS studies, at RT with a scan rate of $5 \text{ mV}\cdot\text{s}^{-1}$. From Figure 9b, the samples demonstrate the ability to sustain higher currents while maintaining the characteristic profile expected for this type of cell [48]. This behavior indicates low internal resistance and reflects the characteristic reversible redox reactions associated to Li-ion intercalation and deintercalation processes.

A similar behavior was observed for LFP-based positive electrodes from C2.1 to C2.6, with a depressed semicircle in the high-frequency zone followed by a tail-line in the low-frequency region (Figure 9c). As mentioned previously, the theoretical fitting is represented by the grayish lines, and the parameters are summarized in Table S2. Accordingly, by EIS analysis and Equation (1), the resistances 141, 6, 49, 37, 2, and 126 Ω were obtained, similar to the ones stated in the literature for similar mass loadings [47,49]. The latter resistances correspond to the ionic conductivities of 0.1, 3.2, 0.4, 0.5, 11.4 and 0.1 $\text{mS}\cdot\text{cm}^{-1}$. The tendency is not clear in Method C2, indicating that the preparation of the positive

electrode may affect the properties of the materials. The application of vacuum led to overall worse ionic conductivities, demonstrating the importance of studying the influence of different parameters on the preparation and performance of LFP-positive electrodes, including drying techniques. In Figure 9d, it is shown that higher loadings stand higher currents. Considering C2 batches, it can be observed that a higher mass loading led to slightly lower resistances, which can lead to enhanced electrochemical behavior [50].

Figure 10 demonstrates the crucial influence of the electrode loading/drying method on the electrochemical performance. In Figure 10a, the six electrodes deliver different specific discharge capacities; as the C-rate increases, a noticeable decline in discharge capacity is observed, primarily attributed to the rise in internal resistance [51]. Among the different samples, there are some observations to highlight: (1) the low-loading electrodes did not demonstrate the best electrochemical performance across the scanned C-rates, (2) at the medium-loading range, a progressive decline in performance was observed for Method C2, with reduced specific discharge capacity and overall efficiency, where the increased mass likely contributed to greater transport limitations. The sample C1.3 surpasses the 100% threshold of CE (Figure S4b), then collapses, which could be related to side reactions, an incomplete charge, or even fluctuations in the Li^+ ion transport during charge–discharge cycles [52], and (3) the best result for Method C was achieved for the electrode with $7.84 \text{ mg}\cdot\text{cm}^{-2}$ (sample C1.5), able to complete higher capacity and to perform at higher C-rates, suggesting an optimal balance between all the electrochemical characterizations so far. However, a further increase in the electrode loading to $9.24 \text{ mg}\cdot\text{cm}^{-2}$ (sample C1.6) led to a significant drop in performance.

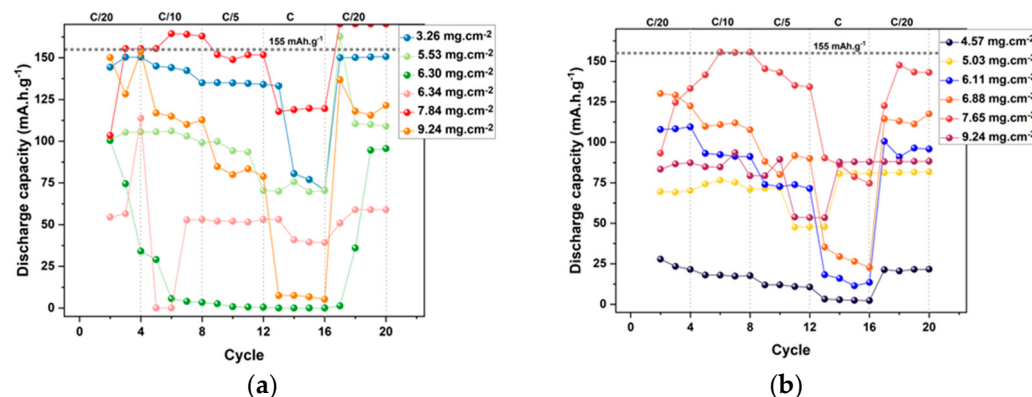


Figure 10. Galvanostatic electrochemical cycling performance at different C–rates and corresponding Coulombic efficiencies for (a) Method C1 (Method C control) and (b) Method C2, respectively.

The same analysis was performed for Method C2. In this case, the preparation process was identical to that of Method C1, with the key difference being the drying method. For Method C2, a vacuum oven was used to dry the positive electrodes, and Figure 10b represents the results for the galvanostatic cycles at different C-rates. In this case, there are key performance trends to discuss: (1) unlike Method C1, the low-loading electrodes delivered inferior electrochemical performance where sample C2.1 and C2.2 showed maximum discharge capacities at the final C/20 scan, with ca. 22 and $82 \text{ mA}\cdot\text{h}\cdot\text{g}^{-1}$, respectively. This can also be demonstrated with the fluctuations in the CE (Figure S4c), far from 100%, as well as in the CV profiles of both samples, (2) the medium-loading electrodes progressively showed better performance, contrarily to what happened in Method C1 and (3) for higher loadings, the best electrochemical performance was achieved with a loading of $7.65 \text{ mg}\cdot\text{cm}^{-2}$, sample C2.5, similarly to all the other methods. However, the performance decreased for the sample with the highest loading, likely due to increased internal resistance.

Overviewing the results obtained with this technique, and in order to make a fair comparison of the best samples of each method, the discharge profiles of samples C1.5 and C2.5 are illustrated in Figure 11. Figure 11a,b show the discharge curves at different C-rates.

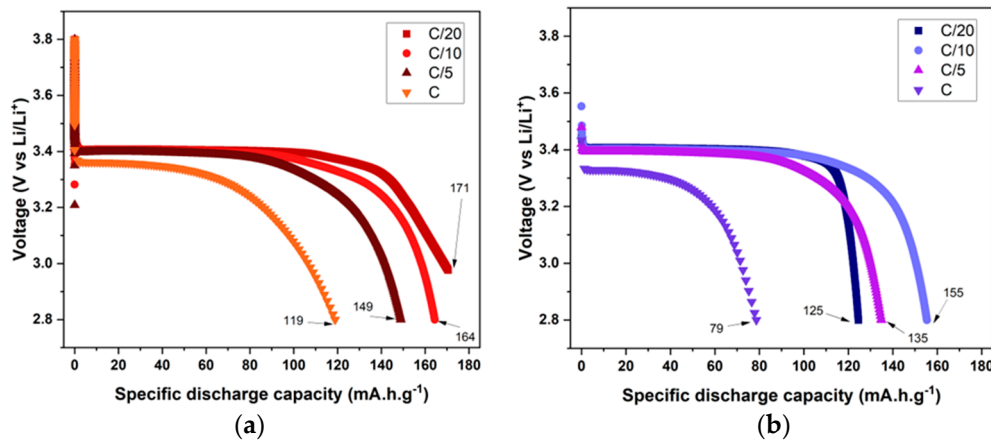


Figure 11. Representative discharge cycles for different C-rates for the best samples prepared by (a) Method C1 (C1.5 with $7.84 \text{ mg}\cdot\text{cm}^{-2}$ and $1.22 \text{ mA}\cdot\text{h}\cdot\text{cm}^{-2}$ areal capacity) and (b) Method C2 (C2.5 with $7.65 \text{ mg}\cdot\text{cm}^{-2}$ and $1.19 \text{ mA}\cdot\text{h}\cdot\text{cm}^{-2}$ areal capacity). The arrows are pointing to the final discharge capacity, in $\text{mA}\cdot\text{h}\cdot\text{g}^{-1}$, of each cycle.

Regarding Figure 11a, sample C1.5 demonstrates the ability to approach the theoretical discharge capacity of LFP at C/20. In this case, the cell reached capacity before reaching the cut-off voltage limit of 2.8 V. In fact, the performance of this sample is well balanced, consistent with observations from previous electrochemical experiments, achieving $119 \text{ mA}\cdot\text{h}\cdot\text{g}^{-1}$ at 1C. These results imply that both preparation steps and drying in Method C1 provided a highly effective electrode for this electrode loading range.

In Figure 11b, the first scan at C/20 shows a lower discharge capacity ($125 \text{ mA}\cdot\text{h}\cdot\text{g}^{-1}$) when compared to C/10 and C/5. This can be attributed to the need for stabilizing the electrode/electrolyte interface, forming a stable solid-electrolyte interphase (SEI) and guaranteeing proper electrolyte wetting within the electrode pores [52]. Although a satisfactory performance was achieved, sample C1.5 ($7.84 \text{ mg}\cdot\text{cm}^{-2}$) yielded better results.

The main focus of this work was to strike a harmonious balance among all indicators of electrochemical behavior. In the Supplementary Materials, Figures S5 and S6 represent the EIS results after electrochemical cycling for each method as well as the logarithm of ionic conductivity as a function of electrode loading before and after electrochemical cycling and the relationship between the specific current at the minimum peak of the CV profiles and the electrode loading of the samples obtained before cycling.

Drawing from these findings, key conclusions emerge and are schematically represented in Figure 12.

From Figure 12, the process of slurry preparation can play a pivotal role in the electrochemical performance. Employing a three-roll mill yielded enhanced outcomes, since this equipment provided a uniform dispersion of particles, owing to the shear stresses and residence time. Furthermore, medium and high electrode loadings exhibited enhanced performance when compared to lower ones, and the vacuum-drying method yielded overall lower electrochemical performance.

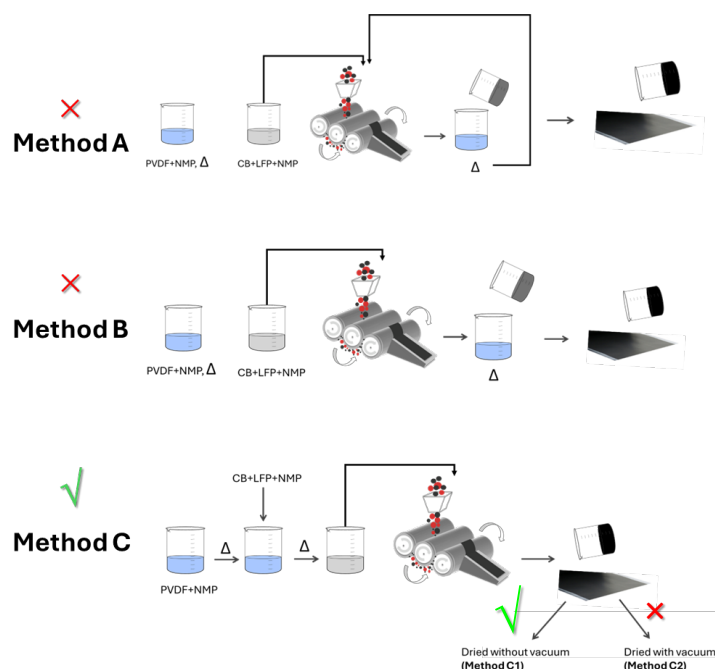


Figure 12. An overview of the dispersion routines and the effect of vacuum drying.

4. Conclusions

This work was focused on studying the impact of process parameters on the performance of LFP-based positive electrodes through systematic investigations into dispersion routines, electrode loadings, and drying processes. Multiple positive electrodes were prepared with a composition of 80 wt.% LFP, 10 wt.% CB, and 10 wt.% PVDF, using a three-roll mill for dispersion. This approach resulted in more uniform and crack-free surfaces, as shown by SEM analysis, and enhanced stability and cyclability in the final devices.

Three different dispersion routines, Methods A, B, and C, were examined by using a three-roll mill and the most suitable (Method C) was used to compare drying modes (Methods C1 and C2). The analysis of the dispersion methods demonstrated that the addition of PVDF in the milling equipment after slurry preparation (Method A) was detrimental, affecting the dispersion quality, which resulted in a decline in discharge capacity and coulombic efficiency, when compared to Methods B and C. Method C = C1, in which a conventional oven was used to post-dry the prepared samples, provided clear evidence of optimized electrochemical performance.

Additionally, among the different prepared electrode loadings, it was found that a medium-loading range ($7\text{--}8 \text{ mg}\cdot\text{cm}^{-2}$, $0.10\text{--}1.24 \text{ mAh}\cdot\text{cm}^{-2}$) resulted in the best overall performance across all the methods explored in this work ($7.5 \text{ mg}\cdot\text{cm}^{-2}$ for A, $6.9 \text{ mg}\cdot\text{cm}^{-2}$ for B, $7.8 \text{ mg}\cdot\text{cm}^{-2}$ for C1, and $7.7 \text{ mg}\cdot\text{cm}^{-2}$ for C2). This could be due to competition between opposed contributions, the ionic and electrical conductivities. On one hand, having a lower load promotes faster ionic conduction in a liquid electrolyte-soaked electrode, but on the other, at a constant electrode thickness, the higher porosity opposes to a fast electrical conductivity, giving rise to an optimal loading range.

An image may arise; like in a “sponge”, the shape and thickness may be preserved but the “free” inner space may be more or less filled, giving rise to an optimal porosity where the charge transfer is faster.

These findings provide a foundation for enhancing the performance of LFP-based positive electrodes by refining the drying methods, adjusting electrode loadings, and optimizing dispersion techniques. Future efforts will explore the enhancement of both ionic

and electrical conductivities through the adjustment of the composition ratio, the potential incorporation of additives, and the improvement of interfacial compatibility.

Supplementary Materials: The following supporting information can be downloaded at: <https://www.mdpi.com/article/10.3390/batteries11030093/s1>, Figure S1: Thickness measurements for samples prepared by Method (a) A, (b) B, (c) C1, and (d) C2; Figure S2: A comparison of the LFP-based positive electrodes' morphologies (secondary electrons): (a) prepared with magnetic agitation ($5000\times$ magnification) without after-(post)-pressure application, and (b) prepared with a milling roll ($5000\times$ magnification) with after-pressure application; Figure S3: Electrochemical characterization of the samples prepared by Method A: (a) electrochemical impedance spectroscopy (EIS), (b) cyclic voltammetry at $5\text{ mV}\cdot\text{s}^{-1}$, (c) galvanostatic cycling, and (d) respective coulombic efficiency; Figure S4: Coulombic efficiencies obtained for Methods (a) B, (b) C1, and (c) C2; Figure S5: EIS results after electrochemical cycling for Methods (a) A, (b) B, (c) C1, and (d) C2; Figure S6: Logarithm of ionic conductivity as a function of electrode loading (a) before and (b) after electrochemical cycling and (c) the relationship between the specific current at the minimum peak (discharge) of the CV profiles and the electrode loading of the samples obtained before cycling. Table S1: Mass of positive electrode components and respective volume of solvent employed for low, medium, and high-loading electrodes. Table S2: Parameters obtained from the equivalent circuit, according to the Modified Restricted Model, for samples prepared by methods A, B, C1, and C2 [53,54].

Author Contributions: Conceptualization, B.A.M., R.M.S. and M.H.B.; methodology, B.A.M., R.M.S. and M.H.B.; investigation, B.A.M.; writing—original draft preparation, B.A.M.; writing—review and editing, all; supervision, M.H.B., R.M.S. and N.C.; project administration, M.H.B., R.M.S. and N.C.; funding acquisition, M.H.B., R.M.S. and N.C. All authors have read and agreed to the published version of the manuscript.

Funding: This research was funded by NGS—New Generation Storage, nr 02/C05-i01.01/2022.PC644 936001-00000045, investment project nr. 58, from the Incentive System to Mobilizing Agendas for Business Innovation, funded by the Recovery and Resilience Plan and by European Funds Next Generation EU. The authors acknowledge Fundação para a Ciência e a Tecnologia (FCT) for its financial support via the project UIDB/50022/2020 (LAETA Base Funding).

Data Availability Statement: The original contributions presented in this study are included in the article and Supplementary Materials. Further inquiries can be directed to the corresponding authors.

Acknowledgments: The authors acknowledge the Serviços de Caracterização de Materiais da Universidade do Minho (SEMAT), Portugal, for the technical support and image acquisition concerning SEM. B.A.M. thanks the Fundação para a Ciência e Tecnologia, Portugal, for the Ph.D. Grant 2023.01813.BD.

Conflicts of Interest: The authors declare no conflicts of interest.

References

1. Guerreiro, A.N.; Maia, B.A.; Khalifa, H.; Baptista, M.C.; Braga, M.H. What Differentiates Dielectric Oxides and Solid Electrolytes on the Pathway toward More Efficient Energy Storage? *Batteries* **2022**, *8*, 232. [[CrossRef](#)]
2. Arshad, F.; Lin, J.; Manurkar, N.; Fan, E.; Ahmad, A.; Tariq, M.-N.; Wu, F.; Chen, R.; Li, L. Life Cycle Assessment of Lithium-Ion Batteries: A Critical Review. *Resour. Conserv. Recycl.* **2022**, *180*, 106164. [[CrossRef](#)]
3. Cui, Z.; Wang, L.; Li, Q.; Wang, K. A Comprehensive Review on the State of Charge Estimation for Lithium-Ion Battery Based on Neural Network. *Int. J. Energy Res.* **2022**, *46*, 5423–5440. [[CrossRef](#)]
4. Tian, J.; Xiong, R.; Shen, W.; Lu, J. State-of-Charge Estimation of LiFePO₄ Batteries in Electric Vehicles: A Deep-Learning Enabled Approach. *Appl. Energy* **2021**, *291*, 116812. [[CrossRef](#)]
5. Chen, Y.; Kang, Y.; Zhao, Y.; Wang, L.; Liu, J.; Li, Y.; Liang, Z.; He, X.; Li, X.; Tavajohi, N.; et al. A Review of Lithium-Ion Battery Safety Concerns: The Issues, Strategies, and Testing Standards. *J. Energy Chem.* **2021**, *59*, 83–99. [[CrossRef](#)]
6. Magalhães, N.; Maia, B.A.; Braga, M.H.; Santos, R.M.; Correia, N.; Cunha, E. Glass Fiber Reinforced Epoxy-Amine Thermosets and Solvate IL: Towards New Composite Polymer Electrolytes for Lithium Battery Applications. *Int. J. Mol. Sci.* **2023**, *24*, 10703. [[CrossRef](#)] [[PubMed](#)]

7. Zhang, C.; Yang, Y.; Liu, X.; Mao, M.; Li, K.; Li, Q.; Zhang, G.; Wang, C. Mobile Energy Storage Technologies for Boosting Carbon Neutrality. *Innovation* **2023**, *4*, 100518. [[CrossRef](#)] [[PubMed](#)]
8. Gao, W.; Liu, C.; Cao, H.; Zheng, X.; Lin, X.; Wang, H.; Zhang, Y.; Sun, Z. Comprehensive Evaluation on Effective Leaching of Critical Metals from Spent Lithium-Ion Batteries. *Waste Manag.* **2018**, *75*, 477–485. [[CrossRef](#)] [[PubMed](#)]
9. Maia, B.A.; Magalhães, N.; Cunha, E.; Braga, M.H.; Santos, R.M.; Correia, N. Designing Versatile Polymers for Lithium-Ion Battery Applications: A Review. *Polymers* **2022**, *14*, 403. [[CrossRef](#)] [[PubMed](#)]
10. Carvalho Baptista, M.; Khalifa, H.; Araújo, A.; Maia, B.A.; Souto, M.; Braga, M.H. Giant Polarization in Quasi-Adiabatic Ferroelectric Na^+ Electrolyte for Solid-State Energy Harvesting and Storage. *Adv. Funct. Mater.* **2023**, *33*, 2212344. [[CrossRef](#)]
11. Xiang, J.; Wei, Y.; Zhong, Y.; Yang, Y.; Cheng, H.; Yuan, L.; Xu, H.; Huang, Y. Building Practical High-Voltage Cathode Materials for Lithium-Ion Batteries. *Adv. Mater.* **2022**, *34*, 2200912. [[CrossRef](#)] [[PubMed](#)]
12. Li, W.; Erickson, E.M.; Manthiram, A. High-Nickel Layered Oxide Cathodes for Lithium-Based Automotive Batteries. *Nat. Energy* **2020**, *5*, 26–34. [[CrossRef](#)]
13. Li, W.; Song, B.; Manthiram, A. High-Voltage Positive Electrode Materials for Lithium-Ion Batteries. *Chem. Soc. Rev.* **2017**, *46*, 3006–3059. [[CrossRef](#)] [[PubMed](#)]
14. Stenina, I.; Minakova, P.; Kulova, T.; Yaroslavtsev, A. Electrochemical Properties of LiFePO_4 Cathodes: The Effect of Carbon Additives. *Batteries* **2022**, *8*, 111. [[CrossRef](#)]
15. Wang, C.; Zhang, R.; Kisslinger, K.; Xin, H.L. Atomic-Scale Observation of O1 Faulted Phase-Induced Deactivation of LiNiO_2 at High Voltage. *Nano Lett.* **2021**, *21*, 3657–3663. [[CrossRef](#)] [[PubMed](#)]
16. Tong, W.; Chu, Q.; Meng, Y.; Wang, X.; Yang, B.; Gao, J.; Zhao, X.; Liu, X. Synthesis of Mesoporous Orthorhombic LiMnO_2 Cathode Materials via a One-Step Flux Method for High Performance Lithium-Ion Batteries. *Mater. Res. Express* **2018**, *5*, 065511. [[CrossRef](#)]
17. Geng, J.; Zhang, S.; Hu, X.; Ling, W.; Peng, X.; Zhong, S.; Liang, F.; Zou, Z. A Review of Graphene-Decorated LiFePO_4 Cathode Materials for Lithium-Ion Batteries. *Ionics* **2022**, *28*, 4899–4922. [[CrossRef](#)]
18. Padhi, A.K.; Nanjundaswamy, K.S.; Goodenough, J.B. LiFePO_4 : A Novel Cathode Material for Rechargeable Batteries. *Proc. Electrochem. Soc. Meet. Abstr.* **1996**, *96*, 73.
19. Padhi, A.K.; Nanjundaswamy, K.S.; Goodenough, J.B. Phospho-olivines as Positive-Electrode Materials for Rechargeable Lithium Batteries. *J. Electrochem. Soc.* **1997**, *144*, 1188. [[CrossRef](#)]
20. Manthiram, A.; Goodenough, J.B. Lithium Insertion into $\text{Fe}_2(\text{MO}_4)_3$ Frameworks: Comparison of M = W with M = Mo. *J. Solid. State Chem.* **1987**, *71*, 349–360. [[CrossRef](#)]
21. Chepurnaya, I.; Smirnova, E.; Karushev, M. Electrochemically Active Polymer Components in Next-Generation LiFePO_4 Cathodes: Can Small Things Make a Big Difference? *Batteries* **2022**, *8*, 185. [[CrossRef](#)]
22. Ahsan, Z.; Ding, B.; Cai, Z.; Wen, C.; Yang, W.; Ma, Y.; Zhang, S.; Song, G.; Javed, M.S. Recent Progress in Capacity Enhancement of LiFePO_4 Cathode for Li-Ion Batteries. *J. Electrochem. Energy Convers. Storage* **2021**, *18*, 10801. [[CrossRef](#)]
23. Zeng, C.; Zheng, R.; Fan, F.; Wang, X.; Tian, G.; Liu, S.; Liu, P.; Wang, C.; Wang, S.; Shu, C. Phase Compatible Surface Engineering to Boost the Cycling Stability of Single-Crystalline Ni-Rich Cathode for High Energy Density Lithium-Ion Batteries. *Energy Storage Mater.* **2024**, *72*, 103788. [[CrossRef](#)]
24. Fan, F.; Zheng, R.; Zeng, T.; Xu, H.; Wen, X.; Wang, X.; Tian, G.; Wang, S.; Zeng, C.; Xiang, W.; et al. Cation-Ordered Ni-Rich Positive Electrode Material with Superior Chemical and Structural Stability Enabled by Atomic Substitution for Lithium-Ion Batteries. *Chem. Eng. J.* **2023**, *477*, 147181. [[CrossRef](#)]
25. Wang, S.; Wen, X.; Huang, Z.; Xu, H.; Fan, F.; Wang, X.; Tian, G.; Liu, S.; Liu, P.; Wang, C.; et al. High-Entropy Strategy Flattening Lithium Ion Migration Energy Landscape to Enhance the Conductivity of Garnet-Type Solid-State Electrolytes. *Adv. Funct. Mater.* **2024**, *2416389*. [[CrossRef](#)]
26. Wang, Y.; Zhang, J.; Xue, J.; Zhang, K.; Wen, L.; Liang, G. Effect of Particle Dispersion on the Properties of LiFePO_4 Slurry and the Electrochemical Properties of the Battery. *Ionics* **2022**, *28*, 1547–1558. [[CrossRef](#)]
27. Katsui, H.; Goto, T. Preparation of Cubic and Tetragonal $\text{Li}_7\text{La}_3\text{Zr}_2\text{O}_{12}$ Film by Metal Organic Chemical Vapor Deposition. *Thin Solid. Films* **2015**, *584*, 130–134. [[CrossRef](#)]
28. Kaiser, J.; Wenzel, V.; Nirschl, H.; Bitsch, B.; Willenbacher, N.; Baunach, M.; Schmitt, M.; Jaiser, S.; Scharfer, P.; Schabel, W. Prozess- und Produktentwicklung von Elektroden für Li-Ionen-Zellen. *Chem. Ing. Tech.* **2014**, *86*, 695–706. [[CrossRef](#)]
29. Nishihora, R.K.; Rachadel, P.L.; Quadri, M.G.N.; Hotza, D. Manufacturing Porous Ceramic Materials by Tape Casting—A Review. *J. Eur. Ceram. Soc.* **2018**, *38*, 988–1001. [[CrossRef](#)]
30. Konda, K.; Moodakare, S.B.; Kumar, P.L.; Battabyal, M.; Seth, J.R.; Juvekar, V.A.; Gopalan, R. Comprehensive Effort on Electrode Slurry Preparation for Better Electrochemical Performance of LiFePO_4 Battery. *J. Power Sources* **2020**, *480*, 228837. [[CrossRef](#)]
31. Orozco-Gallo, D.C.; Vásquez-Arroyave, F.A.; Calderón-Gutiérrez, J.A. Carbon-Slurry Optimization for Lithium-Ion Batteries Customization. *Electrochim. Acta* **2023**, *467*, 143141. [[CrossRef](#)]

32. Folorunso, O.; Sadiku, R.; Hamam, Y. Heteroatom-Doped Carbon Allotropes in Battery Applications. In *Heteroatom-Doped Carbon Allotropes: Progress in Synthesis, Characterization, and Applications*; ACS Symposium Series; American Chemical Society: Washington, DC, USA, 2024; Volume 1491, pp. 105–125.
33. Han, G.; Hu, Q.; Gao, K.; Wang, Y.; Yao, J. LiFe_{0.3}Mn_{0.7}PO₄-on-MXene Heterostructures as Highly Reversible Cathode Materials for Lithium-Ion Batteries. *J. Colloid. Interface Sci.* **2025**, *677*, 513–522. [[CrossRef](#)] [[PubMed](#)]
34. Ye, Z. Performance of Lithium Ion Battery with Graphene Microstructure in Cathode. *J. Phys. Conf. Ser.* **2022**, *2378*, 12030. [[CrossRef](#)]
35. He, S.; Zhang, K.; Zou, Y.; Tian, Z. Three-Dimensional Printed Carbon-Based Microbatteries: Progress on Technologies, Materials and Applications. *New Carbon Mater.* **2022**, *37*, 898–917. [[CrossRef](#)]
36. Liu, T.; Zheng, J.; Hu, H.; Sheng, O.; Ju, Z.; Lu, G.; Liu, Y.; Nai, J.; Wang, Y.; Zhang, W.; et al. In-Situ Construction of a Mg-Modified Interface to Guide Uniform Lithium Deposition for Stable All-Solid-State Batteries. *J. Energy Chem.* **2021**, *55*, 272–278. [[CrossRef](#)]
37. Lee, J.; Pennycook, S.J.; Pantelides, S.T. Simultaneous Enhancement of Electronic and Li⁺ Ion Conductivity in LiFePO₄. *Appl. Phys. Lett.* **2012**, *101*, 33901. [[CrossRef](#)]
38. Kwon, Y.H.; Huie, M.M.; Choi, D.; Chang, M.; Marschilok, A.C.; Takeuchi, K.J.; Takeuchi, E.S.; Reichmanis, E. Toward Uniformly Dispersed Battery Electrode Composite Materials: Characteristics and Performance. *ACS Appl. Mater. Interfaces* **2016**, *8*, 3452–3463. [[CrossRef](#)] [[PubMed](#)]
39. Park, G.; Park, J.-S.; Kim, H.-S.; Lee, K. Preparation of Cathode Slurry for Lithium-Ion Battery by Three-Roll Mill Process. *Carbon Lett.* **2021**, *32*, 265–272. [[CrossRef](#)]
40. Santos, R.M.; Vale, D.; Rocha, J.; Martins, C.; Mould, S.T.; Rocha, N. Multiscale Carbon Fibre-Reinforced Polymer (CFRP) Composites Containing Carbon Nanotubes with Tailored Interfaces. *Fatigue Fract. Eng. Mater. Struct.* **2019**, *42*, 1521–1533. [[CrossRef](#)]
41. Valente, M.; Silva, S.; Braga, M. Cork: Enabler of Sustainable and Efficient Coaxial Structural Batteries. *Heliyon* **2023**, *9*, e15063. [[CrossRef](#)] [[PubMed](#)]
42. Diard, J.-P.; Montella, C. Diffusion-Trapping Impedance under Restricted Linear Diffusion Conditions. *J. Electroanal. Chem.* **2003**, *557*, 19–36. [[CrossRef](#)]
43. Bisquert, J. Influence of the Boundaries in the Impedance of Porous Film Electrodes. *Phys. Chem. Chem. Phys.* **2000**, *2*, 4185–4192. [[CrossRef](#)]
44. Sluyters-Rehbach, M. Impedances of Electrochemical Systems: Terminology, Nomenclature and Representation—Part I: Cells with Metal Electrodes and Liquid Solutions (IUPAC Recommendations 1994). *Pure Appl. Chem.* **1994**, *66*, 1831–1891. [[CrossRef](#)]
45. Baptista, M.C.; Gomes, B.M.; Capela, D.; Ferreira, M.F.S.; Guimarães, D.; Silva, N.A.; Jorge, P.A.S.; Silva, J.J.; Braga, M.H. Conditioning Solid-State Anode-Less Cells for the Next Generation of Batteries. *Batteries* **2023**, *9*, 402. [[CrossRef](#)]
46. Kim, Y.; Kim, M.; Lee, T.; Kim, E.; An, M.; Park, J.; Cho, J.; Son, Y. Investigation of Mass Loading of Cathode Materials for High Energy Lithium-Ion Batteries. *Electrochim. Commun.* **2023**, *147*, 107437. [[CrossRef](#)]
47. Wang, C.; Hong, J. Ionic/Electronic Conducting Characteristics of LiFePO₄ Cathode Materials. *Electrochim. Solid-State Lett.* **2007**, *10*, A65. [[CrossRef](#)]
48. Tolganbek, N.; Zhagalas, N.; Kadyrov, Y.; Umurov, N.; Bakenov, Z.; Mentbayeva, A. Facile Deposition of the LiFePO₄ Cathode by the Electrophoresis Method. *ACS Omega* **2023**, *8*, 8045–8051. [[CrossRef](#)] [[PubMed](#)]
49. Kamenskii, M.A.; Eliseeva, S.N.; Tolstopiatova, E.G.; Volkov, A.I.; Zhuzhelskii, D.V.; Kondratiev, V.V. The Advantages of Mass Normalized Electrochemical Impedance Spectra for the Determination of the Kinetic Parameters of LiMn₂O₄ Cathodes. *Electrochim. Acta* **2019**, *326*, 134969. [[CrossRef](#)]
50. Park, C.-K.; Park, S.-B.; Oh, S.-H.; Ho, J.; Cho, W. Li Ion Diffusivity and Improved Electrochemical Performances of the Carbon Coated LiFePO₄. *Bull. Korean Chem. Soc.* **2011**, *32*, 836–840. [[CrossRef](#)]
51. Zheng, H.; Li, J.; Song, X.; Liu, G.; Battaglia, V.S. A Comprehensive Understanding of Electrode Thickness Effects on the Electrochemical Performances of Li-Ion Battery Cathodes. *Electrochim. Acta* **2012**, *71*, 258–265. [[CrossRef](#)]
52. Gyenes, B.; Stevens, D.A.; Chevrier, V.L.; Dahn, J.R. Understanding Anomalous Behavior in Coulombic Efficiency Measurements on Li-Ion Batteries. *J. Electrochem. Soc.* **2015**, *162*, A278. [[CrossRef](#)]
53. Moya, A.A. Low-Frequency Approximations to the Finite-Length Warburg Diffusion Impedance: The Reflexive Case. *J. Energy Storage* **2024**, *97*, 112911. [[CrossRef](#)]
54. Elgrishi, N.; Rountree, K.J.; McCarthy, B.D.; Rountree, E.S.; Eisenhart, T.T.; Dempsey, J.L. A Practical Beginner’s Guide to Cyclic Voltammetry. *J. Chem. Educ.* **2018**, *95*, 197–206. [[CrossRef](#)]

Disclaimer/Publisher’s Note: The statements, opinions and data contained in all publications are solely those of the individual author(s) and contributor(s) and not of MDPI and/or the editor(s). MDPI and/or the editor(s) disclaim responsibility for any injury to people or property resulting from any ideas, methods, instructions or products referred to in the content.